Acta Mechanica Sinica (2018) 34(6):1015–1034
https://doi.org/10.1007/s10409-018-0792-x

RESEARCH PAPER

An improved boundary element method for modelling a self-reacting point absorber wave energy converter

Qian-Long Xu[1] · Ye Li[1] · Zhi-Liang Lin[1]

Received: 17 October 2017 / Revised: 22 April 2018 / Accepted: 13 May 2018 / Published online: 10 September 2018

Abstract
A numerical model based on a boundary element method (BEM) is developed to predict the performance of two-body self-reacting floating-point absorber (SRFPA) wave energy systems that operate predominantly in heave. The key numerical issues in applying the BEM are systematically discussed. In particular, some improvements and simplifications in the numerical scheme are developed to evaluate the free surface Green's function, which is a main element of difficulty in the BEM. For a locked SRFPA system, the present method is compared with the existing experiment and the Reynolds-averaged Navier–Stokes (RANS)-based method, where it is shown that the inviscid assumption leads to substantial over-prediction of the heave response. For the unlocked SRFPA model we study in this paper, the additional viscous damping primarily induced by flow separation and vortex shedding, is modelled as a quadratic drag force, which is proportional to the square of body velocity. The inclusion of viscous drag in present method significantly improves the prediction of the heave responses and the power absorption performance of the SRFPA system, obtaining results excellent agreement with experimental data and the RANS simulation results over a broad range of incident wave periods, except near resonance in larger wave height scenarios. It is found that the wave overtopping and the re-entering impact of out-of-water floating body are observed more frequently in larger waves, where these non-linear effects are the dominant damping sources and could significantly reduce the power output and the motion responses of the SRFPA system.

Keywords Boundary element method · Floating-point absorber · Heave · Green's function · Viscous drag

1 Introduction

The possibility of utilizing wave energy resources for generating power has gained much interest in recent years. Since Salter [1] published a notable paper about the nodding-duck device, a wide variety of wave energy converter (WEC) designs have been proposed. As one of the simplest WEC devices, the self-reacting floating-point absorber (SRFPA) is widely applied in oceans all over the world. SRFPAs are generally axisymmetric and predominantly operate in heave, extracting energy from the relative motion between two or more bodies. An SRFPA typically consists of two parts, a buoyant, free-surface piercing body referred to as the float and a second free-surface piercing body referred to as the reacting body. When the float reacts against the reacting body in waves, mechanical energy of the induced motion is converted into electricity by a power take-off (PTO) system. The most representative design strategies of the current SRFPA devices can be seen from the OPT PowerBuoy [2], wavebob [3] and inter project service buoy [4–6].

In the numerical simulation of SRFPAs, the hydrodynamic analysis is the focus of research, which can be regarded as a wave-body interaction problem. As the most commonly used approach for predicting the behaviour of ships and offshore structures in waves [7,8], boundary element methods (BEMs) are based on potential flow theory with assumption that the fluid is inviscid, homogeneous, impressible and the flow is irrotational. To model FPAs with more complicated geometries, a frequency domain method is commonly used, where wave excitation forces and hydrodynamic coef-

✉ Ye Li
ye.li@sjtu.edu.cn

[1] State Key Laboratory of Ocean Engineering, Collaborative Innovation Center for Advanced Ship and Deep-Sea Exploration, Muti-function Towing Tank, Key Laboratory of Hydrodynamics (Ministry of Education), School of Naval Architecture, Ocean and Civil Engineering, Shanghai Jiao Tong University, Shanghai 200240, China

ficients are calculated using BEMs that solve radiation and diffraction problems. Then the dynamic response and the power extraction performance of FPAs are obtained by solving the motion equation. Recent works about this can be found in Refs. [9–12]. In the frequency domain method with BEMs, boundary conditions of body surface and free surface are both linearised, which implies that the method is generally limited to relatively small waves and oscillation amplitudes of both the fluid and floating-bodies. Compared to computational fluid dynamics (CFD) methods, although being unable to give reliable prediction for the complex nonlinear hydrodynamic wave-body interaction problems, it can still obtain satisfactory inviscid results with much lower computational cost [13]. Therefore, this approach has been often used in search of resonant frequencies in short time and in the study of optimal tuning and control strategies for FPAs [14–19]. Recently, Sinha et al. [20] used this frequency domain modelling to optimize the power generation performance of heaving FPA arrays in various arrangements.

Overall, most of these frequency domain analyses of the mentioned FPAs were conventionally conducted by the use of commercial BEM-based package WAMIT (developed by the Massachusetts Institute of Technology) [21]. The code WAMIT employs the three-dimensional (3D) free-surface Green's function in frequency domain, which implies that it is only required to distribute singularities with unknown strengths on body surfaces [22] based on the boundary integral equation. The evaluation of the 3D free-surface Green's function is the primary difficulty in applications of the BEM as it is a singular function of complex variable. For the cases of infinite water depth, Newman [23–25] introduced an alternative form of the Cauchy principle value integral and did excellent works on the problem. Based on Newman's work, Yao et al. [26] simplified the numerical scheme of the evaluation and achieved an accuracy of six decimals. For the cases of finite water depth, a series method is preferably used for the evaluation in far field while an integral method is chosen in near field. The work of Newman [24] used the integral method through series expansion and polynomial approximation to gain satisfactory accuracy. Then, work by Chen [27] presented similar approach with the Chebyshev polynomial approximation. However, the approximation intervals should be determined appropriately in their numerical schemes, which restricted the use of corresponding codes in computers.

To model complicated geometries of SRFPAs in waves, this paper systematically describes the numerical methodology in applying the frequency domain analysis with the BEM, as follows: (i) a linear, heave constrained dynamic model with a spring-damper system is used to analyse the power capture performance of SRFPAs; (ii) the boundary-value problems for an SRFPA in waves are specified; (iii) formulation of the classical BEM is presented, and the key numerical issues in the evaluation of the free-surface Green's function are discussed in detail wherein we update the algorithms and simplify the numerical scheme; (iv) the additional viscous damping induced by flow separation and vortex shedding for the SRFPA system is modelled as the quadratic drag force, and we assume that the drag coefficient depends on body geometries and the Keulegan–Carpenter number. Furthermore, the diffraction and radiation problems of a floating hemisphere in waves are analysed to validate the present BEM solver.

The primary objective of this work is to validate the BEM model for predicting motion response and power absorption performance of SRFPA systems. To achieve this, we provide complete comparative analyses of the present method with the experimental measurements and the Reynolds-averaged Navier–Stokes (RANS) simulations from Yu and Li [28] of a locked 1/33-scale model and a unlocked 1/100-scale model over a range of incident wave periods and heights, where the models are inspired by OPT PowerBuoy.

This paper is organized as follows. In Sect. 2, a heave-constrained dynamic model of SRFPA systems in frequency domain is developed (Sect. 2.1); the boundary conditions for the general wave-SRFPA interaction problems and the formulation of the BEM are described (Sect. 2.2); the detailed algorithms for the free surface Green's function are presented in Sect. 2.3; a validation study on the present BEM solver is performed in Sect. 2.4. Sections 3 and 4 present comparative analyses of the present method with existing experimental data and RANS simulations for a locked SRFPA model and a unlocked SRFPA model respectively. In Sect. 5, the power absorption efficiency of the unlocked SRFPA system is discussed. The conclusions are draw in Sect. 6

2 Numerical modelling

2.1 Dynamics

As mentioned, a linear, heave constrained, dynamic model in the frequency domain is used to investigate the motion and power capture of a SRFPA WEC in waves, which contains a linear spring-damper to represent the PTO mechanism. The spatial domain is assumed to have infinite size. A schematic representation of a two-body axisymmetric SRFPA is shown in Fig. 1. Based on Newton's second law, for the rigid two-body system, the constrained heave motion can be written as [29]:

$$\boldsymbol{K}\boldsymbol{z} = \boldsymbol{f}_e, \tag{1}$$

where $\boldsymbol{K}$ is the complex stiffness matrix given by Eq. (2). The wave excitation force in heave mode on body j ($j = 1$ for the float and $j = 2$ for the reacting body) is generally written as

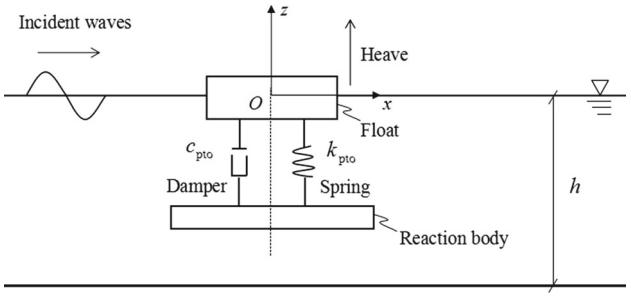

Fig. 1 Schematic representation of an SRFPA model

$F_{ej} = \mathrm{Re}[f_{ej}\mathrm{e}^{-\mathrm{i}\omega t}]$ where f_{ej} and ω are the complex excitation force amplitude and the incident wave frequency. m_j and k_j are the inertia mass and the hydrostatic stiffness of body j. $A_j(\omega)$ and $B_j(\omega)$ represent the added mass and radiation damping of body j in heave. The hydrodynamic radiation coupling term $k_c(\omega)$ between the float and the reacting body, as a small quantity, can be neglected [9,29]. For each body, the wave excitation force and hydrodynamic coefficients are obtained from either BEMs or diffraction and radiation tests in wave tank. The complex amplitudes of body displacements are written as $\boldsymbol{z} = [z_1, z_2]^{\mathrm{T}}$, and the complex velocity amplitudes can be expressed as $u = -\mathrm{i}\omega z$.

$$\boldsymbol{K} = \begin{bmatrix} K_1(\omega) + K_{\mathrm{pto}} & k_c(\omega) - K_{\mathrm{pto}} \\ k_c(\omega) - K_{\mathrm{pto}} & K_2(\omega) + K_{\mathrm{pto}} \end{bmatrix}, \tag{2}$$

$$K_j = -\omega^2[m_j + A_j(\omega)] - \mathrm{i}\omega B_j(\omega) + k_j, \tag{3}$$

$$K_{\mathrm{pto}} = k_{\mathrm{pto}} - \mathrm{i}\omega c_{\mathrm{pto}}, \tag{4}$$

In Eqs. (1)–(4), a spring-damper force $F_{\mathrm{pto}} = \mathrm{Re}[f_{\mathrm{pto}}\mathrm{e}^{-\mathrm{i}\omega t}]$ between the float and the reacting body is quantified as

$$f_{\mathrm{pto}} = -c_{\mathrm{pto}}u_r - k_{\mathrm{pto}}z_r, \tag{5}$$

where k_{pto} is the spring stiffness, c_{pto} is the power absorption damping. $u_r = u_1 - u_2$ and $z_r = z_1 - z_2$ are the relative velocity and displacement between the float and the reacting body, respectively. For this PTO mechanism, the time-averaged power extracted by the SRFPA is equal to the time-averaged power dissipated across the resistance of the PTO, which results in following equation:

$$P = \frac{1}{2}c_{\mathrm{pto}}\|u_r\|^2 = \frac{\omega^2}{2}c_{\mathrm{pto}}\|z_r\|^2. \tag{6}$$

2.2 Hydrodynamics

2.2.1 Boundary-value problems (BVPs)

As defined in Fig. 1, we consider the wave-body interaction problem of the SRFPA model. The water depth for the analysis is h. The spatial domain is assumed to have infinite size. It is supposed that $O - xyz$ is a right-handed Cartesian coordinate system, with $O - xy$ plane coinciding with the undisturbed free surface. Let z-axis lie along the central axis of the SRFPA and be positive upwards against gravity. In the context of potential flow, we can introduce a velocity potential $\Phi(x, y, z, t)$ to express the fluid field, which is defined as

$$\Phi = \mathrm{Re}\left[(\phi_{\mathrm{I}} + \phi_{\mathrm{d}} + u_1\phi_{\mathrm{r1}} + u_2\phi_{\mathrm{r2}})\mathrm{e}^{-\mathrm{i}\omega t}\right], \tag{7}$$

where ϕ_{I} is the incident wave potential; ϕ_{d} is the diffraction potential when these bodies are held fixed; $\phi_{\mathrm{r}j}$ is the unit radiation potential related to the body velocity u_j in heave. With assumption of the linear potential flow theory, the diffraction and radiation potentials satisfy boundary conditions below:

$$\nabla^2\phi_{(\mathrm{d,r})} = 0, \quad (x, y, z) \in \Omega, \tag{8}$$

$$\frac{\partial\phi_{(\mathrm{d,r})}}{\partial z} - \frac{\omega^2}{g}\phi_{(\mathrm{d,r})} = 0, \quad z = 0, \tag{9}$$

$$\frac{\partial\phi_{(\mathrm{d,r})}}{\partial z} = 0, \quad z = -h, \tag{10}$$

$$\phi_{(\mathrm{d,r})} = O\left(\frac{1}{\sqrt{R}}\mathrm{e}^{\mathrm{i}k_0R}\right), \quad R = \sqrt{x^2 + y^2} \to \infty, \tag{11}$$

$$\frac{\partial\phi_{\mathrm{d}}}{\partial n} = -\frac{\partial\phi_{\mathrm{I}}}{\partial n}, \quad \text{on } S_{b1} \ \& \ S_{b2}, \tag{12}$$

$$\frac{\partial\phi_{\mathrm{r1}}}{\partial n} = \begin{cases} n_3, & \text{on } S_{b1}, \\ 0, & \text{on } S_{b2}, \end{cases} \tag{13}$$

$$\frac{\partial\phi_{\mathrm{r2}}}{\partial n} = \begin{cases} 0, & \text{on } S_{b1}, \\ n_3, & \text{on } S_{b2}, \end{cases} \tag{14}$$

where the simplified notation $\phi_{(\mathrm{d,r})}$ denotes the diffraction potential or the radiation potential. Ω represents the whole fluid domain. g is the gravity acceleration. k_0 is the incident wave number. S_{b1} and S_{b2} are the mean wetted surfaces of the float and the reacting body, respectively. $\boldsymbol{n}$ denotes the normal unit vector on body surfaces directed into the float and the reacting body, where n_3 is the Cartesian component along the z-axis.

2.2.2 Boundary element method (BEM)

To solve the BVPs, the boundary integral equation derived from Green's third identity is applied for the evaluation of ϕ_{d} and ϕ_{r}:

$$\alpha(\boldsymbol{p})\phi(\boldsymbol{p}) = \iint_S \left[G(\boldsymbol{p}, \boldsymbol{q})\phi_n(\boldsymbol{q}) - \phi(\boldsymbol{q})G_n(\boldsymbol{p}, \boldsymbol{q})\right]\mathrm{d}s, \tag{15}$$

where $G(\boldsymbol{p}, \boldsymbol{q})$ is the free-surface Green's function with respect to a field point $\boldsymbol{p}(x, y, z)$ and a source point $\boldsymbol{q}(\xi, \eta, \zeta)$. $\alpha(\boldsymbol{p})$ is an interior solid angle at the corresponding point

$\boldsymbol{p}(x, y, z)$ on the body surface $S(S_{b1} + S_{b2})$. Subscript "n" denotes the normal derivative with respect to $\boldsymbol{q}(\xi, \eta, \zeta)$ ($\phi_n = \partial\phi/\partial n_q$, $G_n = \partial G/\partial n_q$). ϕ could be either diffraction potential or radiation potential depending on the BVP to solve.

Letting the field point $\boldsymbol{p}(x, y, z)$ approach to S, we can obtain an integral equation for known ϕ_n and unknown ϕ on S. We discretize the boundary integral equation and subdivide S into a number of small panel elements:

$$S = \sum_{j=1}^{N_e} \triangle S_j, \tag{16}$$

where N_e represents the total number of panel elements on S. These boundary elements can be substituted by planar geometries (quadrilateral or triangular panels). An approximation of constant source and dipole strengths on each panel is made. Thus, the integral equation can be discretized as

$$\sum_{j=1, j\neq i}^{N_e} \phi_j \iint_{\triangle S_j} G_n(\boldsymbol{p}_i, \boldsymbol{q})\mathrm{d}s + 2\pi\phi_i = \sum_{j=1}^{N_e} \phi_{nj} \iint_{\triangle S_j} G(\boldsymbol{p}_i, \boldsymbol{q})\mathrm{d}s, \quad (i, j = 1, 2, \ldots, N_e), \tag{17}$$

where the collocation point $\boldsymbol{p}_i$ is the centroid of the panel $\triangle S_j$. When $i = j$, the solid angle $\alpha(\boldsymbol{p}_i)$ is equal to 2π. In Eqs. (12)–(14), the known ϕ_n is prescribed by boundary conditions. As a consequence, the unknown ϕ on S leads to a system of linear equations as follows

$$\boldsymbol{C}\{\phi\} = \boldsymbol{D}\{\phi_n\}, \tag{18}$$

$$C_{ij} = \iint_{\triangle S_j} G_n(\boldsymbol{p}_i, \boldsymbol{q})\mathrm{d}s \quad (i \neq j), \quad C_{ii} = 2\pi, \tag{19}$$

$$D_{ij} = \iint_{\triangle S_j} G(\boldsymbol{p}_i, \boldsymbol{q})\mathrm{d}s. \tag{20}$$

The system of equations can be solved by a direct or iterative scheme such as the direct Gauss elimination method or the generalized minimum residual method. After determining the radiation and diffraction potentials on body surfaces, the hydrodynamic coefficients and wave excitation forces can be obtained from

$$A_j = \rho \iint_{S_{bj}} \mathrm{Re}\left(\phi_{\mathrm{r}j}\right) n_3 \mathrm{d}s, \tag{21}$$

$$B_j = \rho\omega \iint_{S_{bj}} \mathrm{Im}\left(\phi_{\mathrm{r}j}\right) n_3 \mathrm{d}s, \tag{22}$$

$$f_{ej} = \mathrm{i}\rho\omega \iint_{S_{bj}} \left(\phi_{\mathrm{I}} + \phi_{\mathrm{d}}\right) n_3 \mathrm{d}s, \tag{23}$$

where ρ is the water density. $j = 1$ for the float and $j = 2$ for the reacting body.

2.3 Evaluation of the free-surface Green's function

In the present BEM, it is critical to construct influence coefficient matrices $\boldsymbol{C}$ and $\boldsymbol{D}$. These influence coefficients are virtually integrals of the free-surface Green's function and its normal derivative over panel elements, where the integrals cannot be evaluated analytically. In this section, simplified algorithms for the Green's function are described. The key numerical issues in the construction of influence coefficient matrices are also discussed.

2.3.1 The integral method

An expression of the free-surface Green's function for finite water depth is first given by Wehausen and Laitone [30]:

$$\begin{aligned} G(\boldsymbol{p}, \boldsymbol{q}) = {} & \frac{1}{r} + \frac{1}{\bar{r}} \\ & + \mathrm{P.V.} \int_0^\infty \frac{2(k+\nu)\mathrm{e}^{-kh}\cosh[k(\zeta+h)]\cosh[k(z+h)]}{k\sinh(kh) - \nu\cosh(kh)} \mathrm{J}_0(kR)\mathrm{d}k \\ & + \mathrm{i}2\pi \frac{(k_0+\nu)\mathrm{e}^{-k_0 h}\cosh[k_0(\zeta+h)]\cosh[k_0(z+h)]}{(1-\nu h)\sinh(k_0 h) + k_0 h\cosh(k_0 h)} \mathrm{J}_0(k_0 R), \end{aligned} \tag{24}$$

where

$$\nu = \omega^2/g = k_0 \tanh(k_0 h), \tag{25}$$

$$R = \sqrt{(x-\xi)^2 + (y-\eta)^2}, \tag{26}$$

$$r = \sqrt{R^2 + (z-\zeta)^2}, \quad \bar{r} = \sqrt{R^2 + (z+\zeta+2h)^2}, \tag{27}$$

$\mathrm{J}_0(x)$ is the zero-order Bessel function of the first kind. The wave number k_0, as the only one positive real root of the dispersion relation equation (25), can be extracted by numerical methods.

The main difficulty resides with the evaluation of the third term of the expression (24), where a Cauchy principle-value integral G_c contains a singularity at $k = k_0$. Newman [24] and Chen [27] divided the computational domain ($O - Rz$) into several regions wherein series expansions and polynomial approximations were used for the evaluation. Nevertheless, their numerical schemes were both empirical and complicated, which is difficult for researchers to implement. A direct method to evaluate the principle-value integral using the Gauss–Laguerre quadrature was developed by Endo [31], and Li [32] used it to investigate two ship interactions in shallow water. In reality, Endo's method converges slowly so that much more computational time is needed. To accelerate convergence, we rewrite the principle-value integral as

$$G_c = \text{P.V.} \int_0^\infty \mathrm{e}^{-kh} \left[1 + \frac{2\nu + (k+\nu)\mathrm{e}^{-2kh}}{[k\tanh(kh) - \nu](1+\mathrm{e}^{-2kh})} \right] \bar{E}(k) \mathrm{J}_0(kR) \mathrm{d}k, \tag{28}$$

where

$$\bar{E}(k) = \mathrm{e}^{k(z+\zeta+h)} + \mathrm{e}^{-k(-z+\zeta+h)} + \mathrm{e}^{-k(z-\zeta+h)} + \mathrm{e}^{-k(z+\zeta+3h)}. \tag{29}$$

In Eq. (28), the portion without singularity can be evaluated based on the formula below

$$\int_0^\infty \mathrm{e}^{-ax} \mathrm{J}_0(bx) \mathrm{d}x = (a^2 + b^2)^{-1/2}. \tag{30}$$

While the remaining portion G_c' with a singularity can be represented by

$$G_c' = \text{P.V.} \int_0^\infty \mathrm{e}^{-kh} \frac{f(k)}{g(k)} \mathrm{d}k, \tag{31}$$

where

$$f(k) = \left[2\nu + (k+\nu)\mathrm{e}^{-2kh} \right] \bar{E}(k) \mathrm{J}_0(kR), \tag{32}$$

$$g(k) = [k\tanh(kh) - \nu](1 + \mathrm{e}^{-2kh}). \tag{33}$$

Clearly, $g(k)$ has a first-order zero at $k = k_0$ with the consequence that $f(k)/g(k)$ is no longer bounded, where the Gauss–Laguerre quadrature cannot be applied. To remove singularity, we expand $g(k)$ near $k = k_0$ using the Taylor polynomials with a first-order approximation

$$g(k) \approx g(k_0) + (k - k_0) g'(k_0) = (k - k_0) g'(k_0). \tag{34}$$

Then G_c' becomes

$$G_c' = \int_0^\infty \mathrm{e}^{-kh} \left[\frac{f(k)}{g(k)} - \frac{f(k_0)}{(k-k_0)g'(k_0)} \right] \mathrm{d}k + \frac{f(k_0)}{g'(k_0)} \text{P.V.} \int_0^\infty \frac{\mathrm{e}^{-kh}}{k - k_0} \mathrm{d}k. \tag{35}$$

In Eq. (35), the first integral without singularity can be directly evaluated using the Gauss–Laguerre quadrature, and the second integral is obtained by the exponential integral function [33]

$$G_c' = \sum_{j=1}^{n} w_j \cdot F(x_j) - \frac{f(k_0)}{g'(k_0)} \mathrm{e}^{-k_0 h} \mathrm{E_i}(k_0 h), \tag{36}$$

where w_j is the weight at the j-th Gauss–Laguerre sampling point $x_j = k_j h$; n is the total number of sampling points, and $\mathrm{E_i}(x)$ is the exponential integral function. In addition, analogous to the Green's function $G(\boldsymbol{p}, \boldsymbol{q})$, we implement similar numerical schemes for the evaluation of its partial derivatives $G_R = \partial G/\partial R$ and $G_z = \partial G/\partial z$ [34].

Table 1 Computational results within $h = 10$ m, $\omega = 1$ rad/s, $R = 0.05h$, $\zeta = 0$, $z = -0.01h$, $g = 9.8$ m/s^2

n	G_c	G_{cR}	G_{cz}
10	2.358949	−4.114809	1.202678
20	2.354964	−4.118952	1.202272
30	2.344998	−4.118217	1.201255
100	2.348521	−4.118136	1.201614

Table 2 Computational results within $h = 10$ m, $\omega = 1$ rad/s, $R = 0.05h$, $\zeta = 0$, $z = -0.05h$, $g = 9.8$ m/s^2

n	G_c	G_{cR}	G_{cz}
10	1.646718	−1.542709	1.733955
20	1.647111	−1.543346	1.733995
30	1.646784	−1.543329	1.733962
100	1.646806	−1.543327	1.733964

Table 3 Computational results within $h = 10$ m, $\omega = 1$ rad/s, $R = 0.05h$, $\zeta = 0$, $z = -0.1h$, $g = 9.8$ m/s^2

n	G_c	G_{cR}	G_{cz}
10	1.000135	−0.406281	0.916077
20	1.000243	−0.406348	0.916088
30	1.000238	−0.406348	0.916088
100	1.000238	−0.406348	0.916088

Tables 1–3 list the computational values of G_c and its partial derivatives G_{cR}, G_{cz} with different number of the Gauss–Laguerre sampling points. First, the results show that the present method converges well as the number of sampling points increases. Second, the parameter z has an influence on the numerical convergence: the present method converges faster as the absolute value of z increases. Because $G(\boldsymbol{p}, \boldsymbol{q}) \equiv G(\boldsymbol{q}, \boldsymbol{p})$, it is clear that the parameter ζ has the same influence on it as z. To keep balance between the numerical accuracy and the computational efficiency, 30 Gauss–Laguerre sampling points are used for the evaluation of G, G_R and G_z in the present BEM.

2.3.2 The series method

Alternatively, the free-surface Green's function can be expressed in term of an infinite-series expansion, which was derived from John [35]:

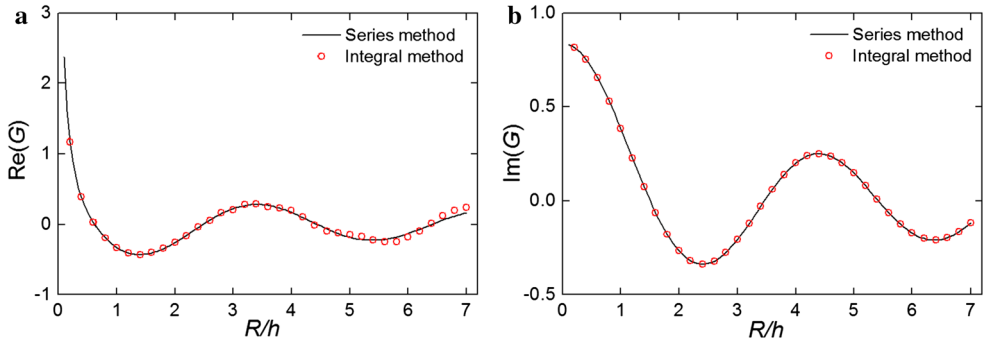

Fig. 2 Comparison of the computational values of G between the series method and the integral method in the case $h = 10$ m, $\omega = 1.2$ rad/s, $z = \zeta = -0.01h$. **a** Real part. **b** Imaginary part

$$G(\boldsymbol{p},\boldsymbol{q}) = 4\sum_{n=1}^{\infty}\frac{k_n^2+\nu^2}{h(k_n^2+\nu^2)-\nu}\cos[k_n(\zeta+h)]\cos[k_n(z+h)]\mathrm{K}_0(k_nR) - \mathrm{i}2\pi\frac{\nu^2-k_0^2}{h(k_0^2-\nu^2)+\nu}\cosh[k_0(\zeta+h)]\cosh[k_0(z+h)]\mathrm{H}_0^{(1)}(k_0R), \tag{37}$$

where $\mathrm{K}_0(x)$ is the zero-order modified Bessel function of the second kind. $\mathrm{H}_0^{(1)}(x)$ is the zero-order Hankel function of the first kind. k_n denotes the n-th positive real root of

$$k\tan(kh) = -\nu. \tag{38}$$

It is worthwhile to note that

$$(n-1/2)\pi \leqslant k_nh \leqslant n\pi, \quad n = 1, 2, \ldots, \infty. \tag{39}$$

For small n, these roots can be extracted by the bisection method or the Newton downhill method. In addition, for large n, $k_n \approx n\pi/h$. The asymptotic expansion series of the m-order Bessel function $\mathrm{K_m}(x)$ is used here

$$\mathrm{K_m}(x) = \frac{\pi}{2\sqrt{x}}\mathrm{e}^{-x}, \quad x \to \infty, \quad m = 0, 1, 2, \ldots, \infty. \tag{40}$$

Based on Eq. (40), for large n we can have

$$\mathrm{K}_0(k_nR) = O\left(\mathrm{e}^{-n\pi R/h}\right). \tag{41}$$

Thus, we can conclude that the convergence of this series primarily depends on the ratio R/h, and the number of series terms required for a given accuracy is proportional to h/R. Compared to the integral method, the series method is preferable in the far-field (large values of R/h). However, it is useless for small values of R/h, since each series term contains a logarithmic singularity ($\mathrm{K}_0(x) \to \infty$) when $R/h = 0$, so only the integral method is feasible for small values of R/h. In addition, algorithms for the partial derivatives G_R and G_z are analogous to G.

A comparison of the real and the imaginary parts of the computational values of G obtained from the present integral method with these obtained from the series method is made in Fig. 2a, b. The Green's function is evaluated for the case $h = 10$ m, $\omega = 1.2$ rad/s, $z = \zeta = -0.01h$. The test was conducted using the FORTRAN compiler on a 4 GHz Intel i7-4790K processor. Thirty Gauss–Laguerre sampling points are used in the integral scheme and the series expansion is truncated when it achieves an accuracy of six decimals in the series scheme. As can be seen from Fig. 2, the results are virtually identical.

The total CPU time consumed in the evaluation of G, G_R and G_z for two cases: (i) $h = 10$ m, $\omega = 1.2$ rad/s, $z = \zeta = -0.01h$; (ii) $h = 20$ m, $\omega = 0.8$ rad/s, $z = \zeta = -0.2h$, is shown in Fig. 3a, b, for numerical tests across the 0.02–5 range of the ratio R/h. In different cases, similar results are observed in Fig. 3a, b. This indicates that parameters h, ω, z and ζ have little effect on the computational speed for both the integral scheme and the series scheme. For the integral method, an increase in the ratio R/h tends to increase the total computational time. A converse trend is evident for the series method, especially below $R/h = 0.1$: the computational time increases rapidly with decreasing ratio R/h. Clearly, due to the singularity of the Bessel function $\mathrm{K_m}(x)$, the series method converges slowly when the ratio R/h approaches zero, which consequently results in increasing computational time. While the trend of CPU time consumed in the integral scheme with increasing ratio R/h is explainable by considering that the evaluation of the Bessel function $\mathrm{J_m}(x)$ costs more running time for larger ratio R/h.

A critical value 0.1 of the ratio R/h can be observed in Fig. 3a, b. The integral method exhibits much higher computational efficiency below 0.1, and the series method costs much less running time above 0.1. Therefore, an optimized strategy that the integral scheme implemented for $R/h < 0.1$ and the series scheme implemented for $R/h > 0.1$ is adopted in the present BEM.

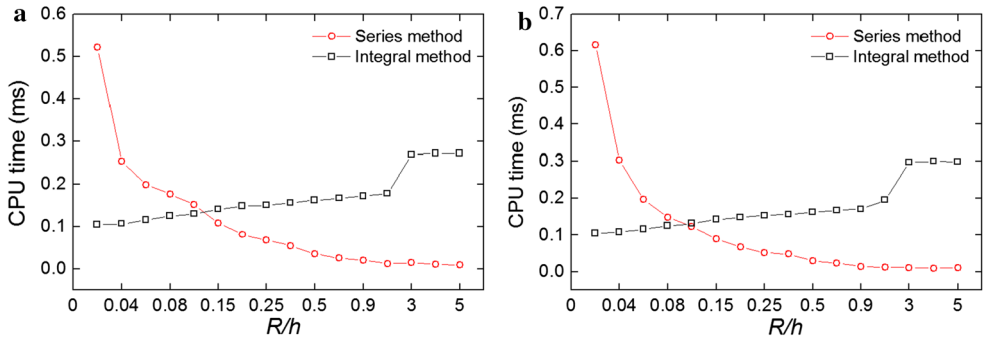

Fig. 3 Total CPU time in the evaluation of G, G_R and G_z in two cases. **a** $h = 10$ m, $\omega = 1.2$ rad/s, $z = \zeta = -0.01h$. **b** $h = 20$ m, $\omega = 0.8$ rad/s, $z = \zeta = -0.2h$

2.3.3 Deep water cases

As is well known, when the wavelength λ is small compared to the water depth h (large ratio h/λ), it can be deemed a deep water wave. In these cases, distorted computations of the free-surface Green's function and its partial derivatives frequently arise in the numerical schemes. To overcome it, the free-surface Green's function in infinite water depth is introduced here, and it can be expressed as

$$G(\boldsymbol{p},\boldsymbol{q}) = \frac{1}{r} + \frac{1}{\bar{r}} + 2\nu \mathrm{P.V.}\int_0^\infty \frac{\mathrm{e}^{k(z+\zeta)}}{k-\nu}\mathrm{J}_0(kR)\mathrm{d}k + \mathrm{i}2\pi\nu \mathrm{e}^{\nu(z+\zeta)}\mathrm{J}_0(\nu R), \tag{42}$$

where

$$r = \sqrt{R^2 + (z-\zeta)^2}, \quad \bar{r} = \sqrt{R^2 + (z+\zeta)^2}. \tag{43}$$

The expression (42) was the first derived by Havelock [36]. The main difficulty resides with the evaluation of the third term of the expression, where a Cauchy principle-value integral contains a singularity at $k = \nu$. To solve this problem, Yao et al. [26] developed a simplified algorithm to gain at least an accuracy of 6 decimals, wherein series expansion and Gauss–Legendre quadrature were used in sub-domains ($O - Rz$). For deep water cases, Sun's algorithm for the Green's function and its partial derivatives is adopted in the present BEM. The detailed algorithm can be found in Ref. [26].

2.3.4 Influence coefficients

As seen in Eqs. (24), (37) and (42), the free surface Green's function $G(\boldsymbol{p},\boldsymbol{q})$ can be represented by the Rankin source Green's function and the remaining portion: $G = 1/r + G'$, then the influence coefficients can be written as

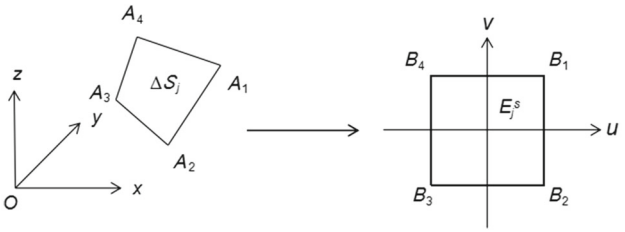

Fig. 4 A generic four-node quadrilateral element and its projection in the parametric space ($u \in [-1, 1]$, $v \in [-1, 1]$)

$$C_{ij} = \iint_{\triangle S_j} \frac{\partial(1/r)}{\partial n}\mathrm{d}s + \iint_{\triangle S_j} G'_n(\boldsymbol{p}_i,\boldsymbol{q})\mathrm{d}s \quad (i \neq j), \tag{44}$$

$$D_{ij} = \iint_{\triangle S_j} \frac{1}{r}\mathrm{d}s + \iint_{\triangle S_j} G'(\boldsymbol{p}_i,\boldsymbol{q})\mathrm{d}s, \tag{45}$$

Because of the singularity of $1/r$ when $\boldsymbol{p}_i$ approaches to $\boldsymbol{q}$ on the element $\triangle S_i$, the integrals of the Rankin source Green's function in Eqs. (44) and (45) have to be evaluated analytically [37]. The remaining portion G' and its normal derivatives G'_n can be directly integrated on each panel element using the two-dimensional Gauss–Legendre quadrature. To implement it, every four-node quadrilateral element $\triangle S_j$ should be mapped to a standard square E_j^s ($u \in [-1, 1]$, $v \in [-1, 1]$) in a parametric space, as shown in Fig. 4.

Thus, the influence coefficients can be evaluated by

$$\begin{aligned}
\iint_{\triangle S_j} G'_n(\boldsymbol{p}_i,\boldsymbol{q})\mathrm{d}s &= \int_{-1}^{1}\int_{-1}^{1} f(u,v)\mathrm{d}u\mathrm{d}v \\
&= \sum_{k=1}^{n}\sum_{l=1}^{n} w_k w_l f(u_k, v_l), \\
\iint_{\triangle S_j} G'(\boldsymbol{p}_i,\boldsymbol{q})\mathrm{d}s &= \int_{-1}^{1}\int_{-1}^{1} g(u,v)\mathrm{d}u\mathrm{d}v \\
&= \sum_{k=1}^{n}\sum_{l=1}^{n} w_k w_l g(u_k, v_l),
\end{aligned} \tag{46}$$

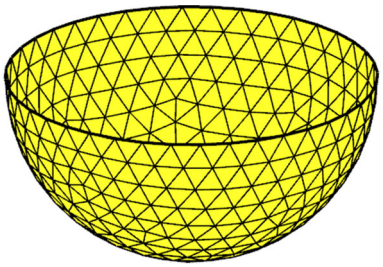

Fig. 5 Panel meshes (triangle elements) used for BEM analysis of a hemisphere

where

$$f(u,v) = G'_n\left(\boldsymbol{p}_i(x_i,y_i,z_i), \boldsymbol{q}[\xi(u,v),\eta(u,v),\zeta(u,v)]\right) J(u,v),$$
$$g(u,v) = G'\left(\boldsymbol{p}_i(x_i,y_i,z_i), \boldsymbol{q}[\xi(u,v),\eta(u,v),\zeta(u,v)]\right) J(u,v). \tag{47}$$

For triangular elements, Eq. (46) is rewritten as

$$\iint_{\triangle S_j} G'_n(\boldsymbol{p}_i,\boldsymbol{q})\mathrm{d}s = \sum_{k=1}^{n}\sum_{l=1}^{n} R_k w_k w_l f(u_k,v_l),$$
$$\iint_{\triangle S_j} G'(\boldsymbol{p}_i,\boldsymbol{q})\mathrm{d}s = \sum_{k=1}^{n}\sum_{l=1}^{n} R_k w_k w_l g(u_k,v_l), \tag{48}$$

where

$$v_l = \frac{1}{2}(1+u_k) + \frac{1}{2}(1-u_k)u_l. \qquad R_k = \frac{1}{2}(1-u_k). \tag{49}$$

In Eqs. (46)–(49), w_k is the weight at the k-th Gauss–Legendre sampling point u_k in $u \in [-1,1]$, and w_l is the weight at the l-th sampling point v_l in $v \in [-1,1]$. n is the number of sampling points used in the Gauss–Legendre quadrature. $J(u,v)$ is the Jacobian determinant. The detailed transformation relation between $\triangle S_j$ and E_j^s is given in the Appendix.

Apparently, the influence coefficients can be evaluated numerically using the values of the Green's function and its normal derivative at the sampling points on panel elements. The computational accuracy depends on the number of sampling points used in the Gauss–Legendre quadrature. In general, for small panel elements, satisfactory results can be obtained when at least four sampling points ($n = 2$) are used.

2.4 BEM validation

In this section, an example concerning the diffraction-radiation problem of a floating hemisphere with radius $R_0 = 1$ is investigated to validate the present BEM algorithm. As shown in Fig. 5, the wetted surface of the hemisphere is discretized by 610 triangular panel elements with 326 nodes. The numerical test is performed for 100 wave frequencies across a range of $k_0 R_0$ varying from 0 to 10.

Both the added mass m_a and radiation damping B_d in heave can be determined according to the analytical solution for a floating hemisphere derived from Hulme [38]:

$$m_a(\omega) = \frac{2}{3}\rho\pi R_0^3 a_{33}, \quad B_d(\omega) = \frac{2}{3}\rho\pi R_0^3 \omega b_{33}, \tag{50}$$

where ρ is the water density. a_{33} and b_{33} are the heave added mass and radiation damping coefficients, respectively. These results of a_{33} and b_{33} obtained from the present BEM and Hulme are reported in Fig. 6a, b.

The complex wave excitation force f_e on the floating hemisphere in heave is derived by Chen et al. [39] using a numerical approach:

$$f_e(\omega) = \rho g \pi R_0^3 f_3, \tag{51}$$

where the real and imaginary parts of the heave force coefficient f_3 obtained from the present BEM and Chen et al. are reported in Fig. 7a, b, respectively. It is noted that the theoretical solutions for a hemisphere from Hulme [38] and Chen et al. [39] refer to deep water conditions, and are believed to be accurate from two up to four decimal places based on their studies.

By comparison, it is evident that the present calculations agree well with the available results, which proves that the proposed BEM can accurately provide inviscid hydrodynamic results of floating bodies in waves.

3 Locked SRFPA modelling

Generally, in extreme wave scenarios, SRFPAs are automatically locked to increase survivability such that no relative motion occurs between the float and the reaction body. In this section, a series of studies is first performed by using a locked SRFPA without the consideration of power extraction. As discussed in Sect. 2.1, the heave constrained motion equation for it is formulated as a single body:

$$\left[-\omega^2(m + A(\omega)) - \mathrm{i}\omega B(\omega) + k\right] z = f_e, \tag{52}$$

where $A(\omega)$ and $B(\omega)$ are added mass and radiation damping in heave; k is the hydrostatic stiffness; f_e is the wave excitation force complex amplitude in heave on the locked model; z is the complex amplitude of heave displacement. In addition, an experimental heave decay test and a RANS simulation of the locked SRFPA model in waves were conducted

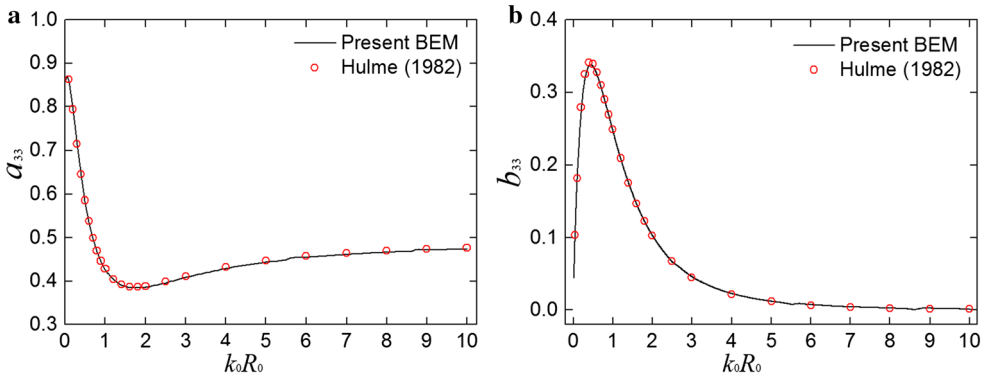

Fig. 6 **a** Added mass. **b** Radiation damping coefficients of a hemisphere in heave

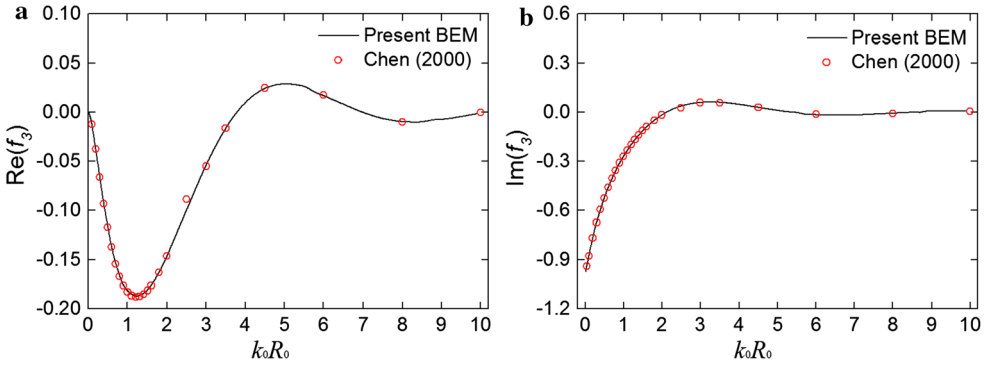

Fig. 7 Complex wave excitation force. **a** Real part. **b** Imaginary part on a hemisphere in heave

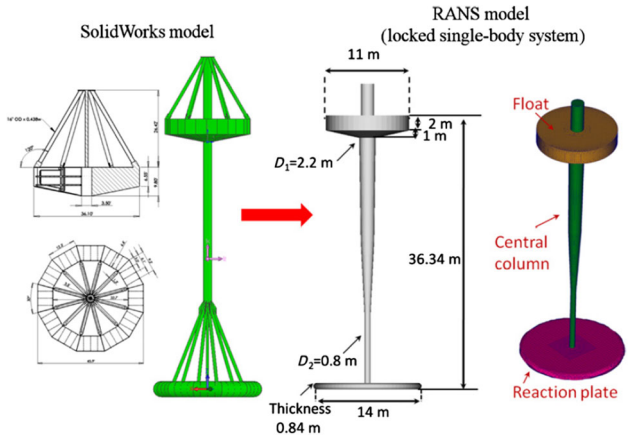

Fig. 8 Locked SRFPA geometry and dimension in the heave decay test and the RANS simulation

by Yu and Li [28]. The data is used to validate the numerical dynamic model.

3.1 SRFPA geometry and dimension

Figure 8 shows the geometry and the dimension of the locked SRFPA model used in the heave decay test and the RANS simulation. In the RANS simulation, only a basic structural design was considered, where the model geometry neglected the supporting jacket and the details of the reaction plate. A same model was used in the present BEM, and the top central column was neglected. The inertial mass of full-scale model used in the present BEM and the RANS simulation is about 250 metric tons with the gravity center located 22.4 m below the still free surface.

3.2 Radiation problem and heave decay test

3.2.1 Radiation problem analysis

The present BEM code is used to obtain the inviscid hydrodynamic coefficients of the locked SRFPA model in heave. The panel meshes used in the calculation are shown in Fig. 9, which include 1864 panel elements with 1744 nodes. The water depth for the analysis is 150 m.

The added mass normalized by the model's inertial mass derived from the BEM is plotted in Fig. 10a, for the calculation across the 6–18 s range of oscillation periods. Key observations of the results are as follows. First, the added mass in heave exhibits a very slight increase with oscillation period, which indicates that the oscillation period has little effect on the added mass. Second, the added mass is about four to five times the model's inertial mass (250 tons)

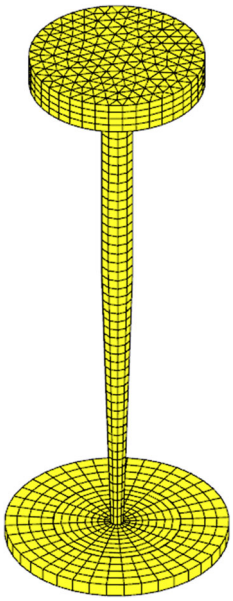

Fig. 9 Panel meshes used for BEM analysis of the locked SRFPA

in operational oscillation periods. It is clear that, as a damper plate, the reaction plate of the locked SRFPA provides a much larger added mass effect because it pulls and pushes a large volume of fluid during the heave motion.

The radiation damping derived from the BEM is shown in Fig. 10b, across the same range of oscillation periods. The results show that an increase in oscillation period decreases the radiation damping obviously. Since the wave radiation is a free-surface phenomenon, and the reaction plate lies far from the free surface, the radiation damping on the reaction plate is in fact negligible and the float provides a primary radiation damping effect, which is also proved in Sect. 4.

3.2.2 Heave decay test

The heave decay test was conducted at UC Berkeley's wave tank, where a 1/100-scale model was built based on the full-scale Solidworks design. More details of the experimental design and settings are described in Ref. [28].

In the frequency domain analysis, the heave decay of a floating body can be considered a radiation problem at its natural frequency. For the locked SRFPA, if the initial velocity is assumed to be zero, its heave decay equation can be expressed as

$$Z(t) = Z_0 \mathrm{e}^{-\delta t} \cos(\omega_r t), \tag{53}$$

where

$$\delta = -\frac{B(\omega_r)}{2[m + A(\omega_r)]}, \qquad \omega_r = \sqrt{\frac{k}{m + A(\omega_r)}}, \tag{54}$$

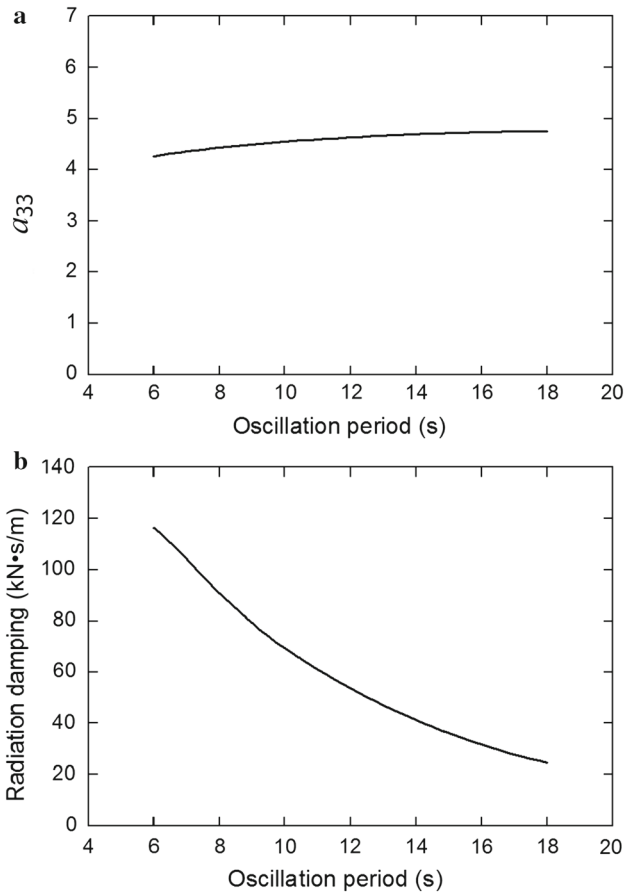

Fig. 10 BEM derived. **a** Added mass. **b** Radiation damping coefficients in heave as a function of oscillation period

Z_0 is the initial displacement of the model; ω_r is the natural frequency in heave; $A(\omega_r)$ and $B(\omega_r)$ are added mass and radiation damping of the model at its natural frequency, respectively.

Based on the BEM-derived added mass, the natural frequency of the model (full scale) in heave can be determined by the intersection of two curves plotted in Fig. 11, where the natural frequency is found to be around 0.7 rad/s. Figure 12 shows the heave decay time history obtained from the present BEM analysis in frequency domain and the experimental measurement. Two key observations are made by comparing these results. First, from the experimental data, the natural decay period is found to be around 9 s, which agrees well with the BEM analysis. Second, a faster decay of heave amplitude is observed in the experiment. As seen in Eq. (54), the natural frequency depends on the hydrostatic stiffness, inertial mass and added mass. The hydrostatic stiffness and inertial mass of the locked SRFPA were adjusted to match the experimental decay test. It is apparent, therefore, that the added mass at the natural frequency is well predicted by the present BEM analysis because fluid inertial forces are generally well defined by potential flow theory within

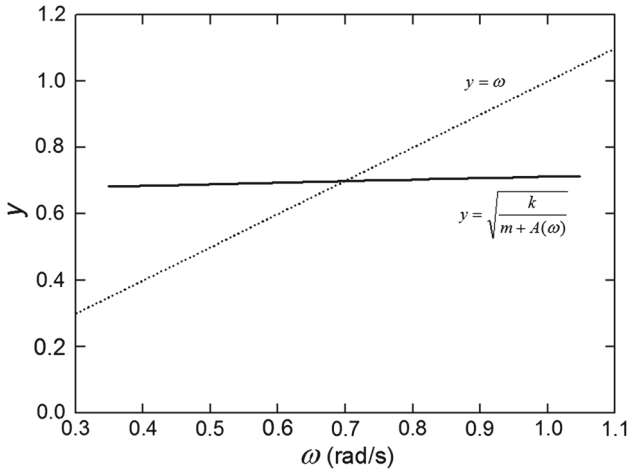

Fig. 11 Determination of the natural frequency of the Locked SRFPA model in heave

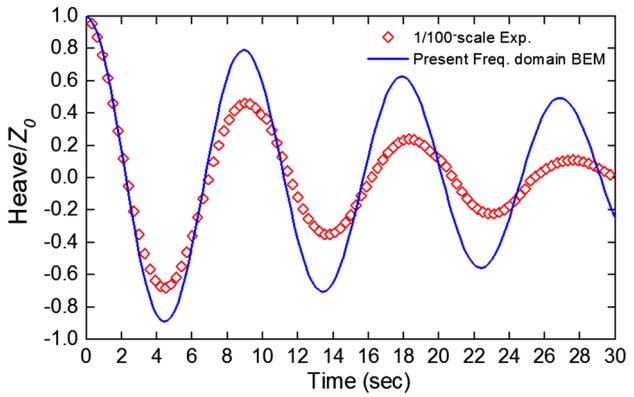

Fig. 12 Heave decay results from the BEM in frequency domain and the experimental measurement (full scale)

the BEM. However, a faster heave decay indicates that the damping on the model in the experiment is greater than the BEM-derived damping. It is probable that viscous damping has a significant effect on the heave decay process, while the BEM analysis only accounts for the damping effect from wave radiation but does not account for these viscous effects.

3.3 Heave response in waves

A series of RANS simulations was performed to investigate the interaction between regular waves and the locked SRFPA in water depth 70 m using a commercial CFD package STAR-CCM+ [28], where the meshes with 1.6 million elements were created. A 5th-order Stokes wave velocity profile was specified at the inflow boundary to provide various wave scenarios. The panel meshes used in the BEM analysis are the same as those shown in Fig. 9. The heave response amplitude operators (RAOs) obtained from the present BEM and the RANS simulations in two different incident wave heights, 2 m and 4 m, are plotted in Fig. 13.

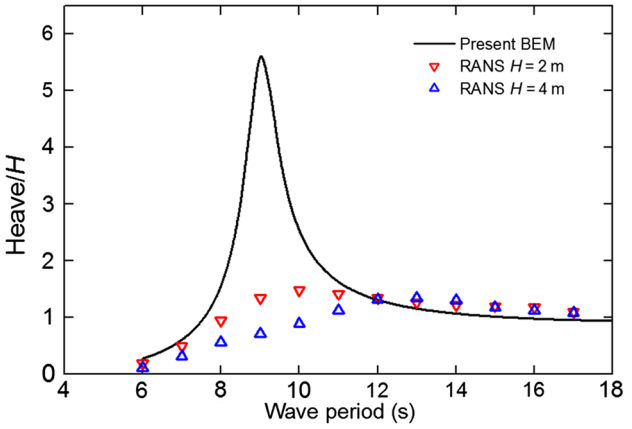

Fig. 13 Comparison of the heave RAOs (scaled by wave height H) in regular waves

As shown in Fig. 13, key observations are made as follows. First, satisfactory agreement can be seen between the heave response derived from the dynamic model with BEM and the RANS simulations at wave periods below 7 s and above 12 s, but the dynamic model with BEM heavily over-predicts the heave response near resonance. Second, the same trends of RAOs from the BEM analysis and the RANS simulations are observed; the RAO under 2 m wave height has a peak period 10 s close to the natural period obtained from the BEM analysis; the heave amplitude is reduced near resonance and the peak period shifts to about 13 s under 4 m wave height compared to 2 m wave height scenarios.

Interpreting the RAO results from the BEM and the RANS method yields the following points. First, because the dynamic model with the present BEM in this paper is a linear model, it does not account for the wave amplitude dependence in the RANS simulations. Second, for operational wave conditions, when the wave period is sufficiently longer or shorter than the resonant period, linear effects on the interaction between waves and the locked SRFPA are dominant while viscous effects are negligible. Therefore, the inviscid BEM analysis can exhibit satisfactory agreement of RAO results with the RANS simulations under different wave heights at wave periods below 7 s and above 12 s. Third, near resonance, the locked SRFPA exhibits fierce motion and a much lager motion amplitude can be anticipated. In this scenario, viscous effects are the dominant source of damping for the SRFPA, particularly the viscous drag, as a result of flow separation and vortex shedding for the float and reaction plate, which greatly reduce the heave response amplitude. Meanwhile, the nonlinear effects on the interaction between waves and the SRFPA is quite significant, which may introduce additional damping forces that reduce motion amplitude as well. However, these issues are not accounted for in the dynamic model with the BEM, which leads to over-prediction of heave response near resonance. Fourth, the reduced motion

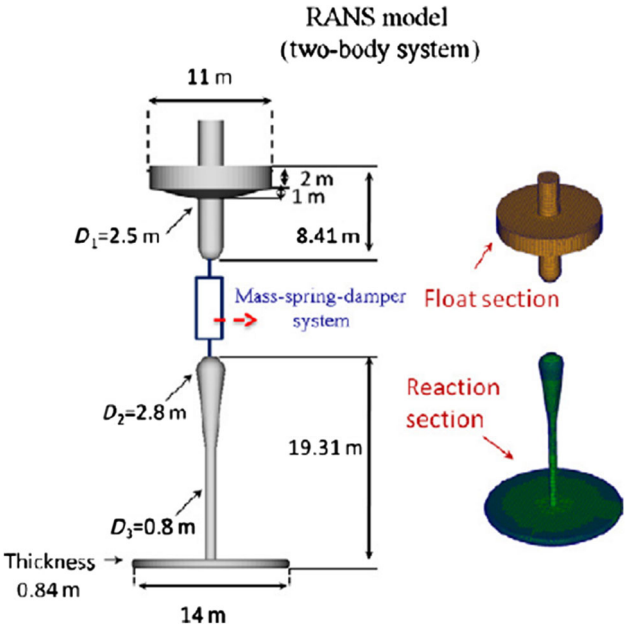

Fig. 14 Two-body SRFPA model in RANS

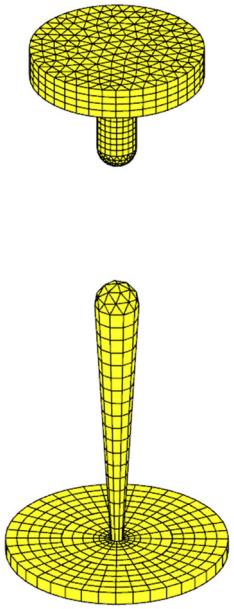

Fig. 15 Panel meshes used for BEM analysis of the SRFPA

amplitude and the shift of the peak period under 4 m wave height indicate that the SRFPA is subject to a larger damping in lager wave height scenarios. Note that wave overtopping barely occurred under 2 m wave height in the RANS simulations, but it was frequently observed in the 4 m wave height scenarios. As a result, it is anticipated that wave overtopping may result in an additional damping force to restrain the SRFPA motion. In summary, by comparison of the RAO results, notable differences near resonance attributed to these viscous and nonlinear effects discussed, illustrate that the inclusion of these effects within the total damping are critical to the validity of the numerical model with the present BEM. In the following section, an additional nonlinear drag force term will be introduced into the numerical dynamic model, which will be used to investigate the motion response and power generation of SRFPAs.

4 Two-body SRFPA in waves

The dynamics and hydrodynamics with the present BEM of the two-body SRFPA system have been discussed in Sect. 2, where the power generation depends on the relative motion between the float and the reaction body. By introducing a viscous drag term to the dynamic model, a series of the BEM analyses is performed to investigate the motion response and power extraction potential of the SRFPA system. Note that the investigation is not focused on the optimal control strategy. The results are compared with the experimental measurements and RANS simulation results [28] for validation.

4.1 SRFPA geometry and settings

Figure 14 shows the geometry and dimension of the two-body SRFPA system used in the RANS simulation, where the numerical settings and the mesh resolution are similar to those applied in the locked SRFPA simulations. Similar geometry and dimension were set in the BEM analysis, and the top central column of the float was neglected. Figure 15 shows the panel meshes used in the BEM calculation, which include 1940 panel elements with 1719 nodes. As seen in Fig. 14, the reaction section is fully submerged and keeps neutrally buoyant. The float and the reaction section weigh 84.5 metric tons and 165 metric tons respectively, and they are connected by a mass-spring-damper system which is applied to provide the PTO mechanism of the dynamics model discussed in Sect. 2.1. The spring is mainly utilized to connect the two sections and a small stiffness 20 kN/m is specified to keep the reaction section in initial equilibrium. The power absorption damping is a specified constant in each numerical simulation.

4.2 Wave tank test

An experimental test of the SRFPA was performed using a wave tank at UC San Diego Scripps Institution of Oceanography's, where a 1/33-scale model was used in the experiment. More details of the experimental design and settings are described in Ref. [40]. The float and the reaction section were connected to a miniature hydraulic cylinder in closed circuits with a needle valve to provide power absorption damping to represent the PTO mechanism, where the damping is controlled by turning the needle valve.

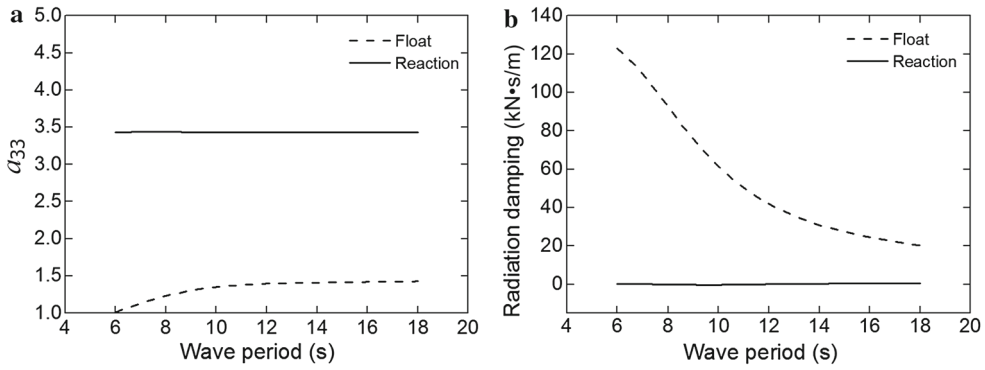

Fig. 16 BEM derived. **a** Added mass. **b** Radiation damping of the SRFPA

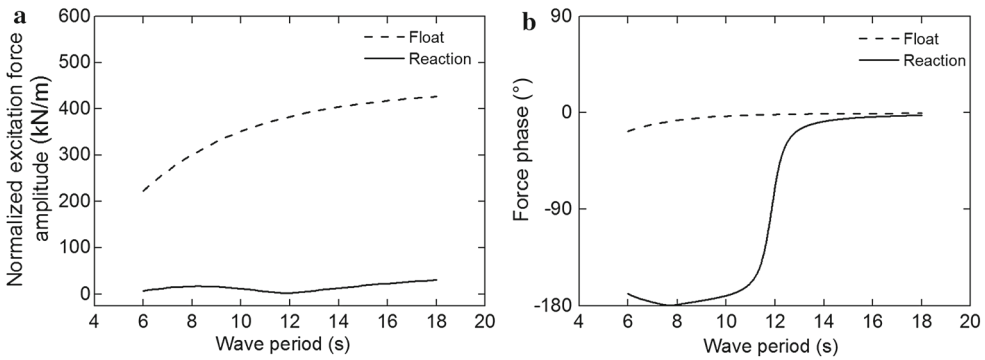

Fig. 17 BEM derived excitation force. **a** Amplitude. **b** Phase on the SRFPA

4.3 Radiation and diffraction problem analyses

Based on the BVPs discussed in Sect. 2.2.1, the radiation and diffraction analyses of the SRFPA are performed using the present BEM, where hydrodynamic effects of the float and reaction section are assessed in the presence of the other body. For each body, the added mass, radiation damping and excitation force in heave are obtained, for the calculation across the 6–18 s range of wave periods.

The added mass normalized by the total inertial mass (249.5 metric tons) of the SRFPA is shown in Fig. 16a. First, the added mass for the float increases slightly with wave period, whereas, for the reaction section, results exhibit no variation. This indicates that the wave period has little effect on the added mass of the SRFPA system. Second, the added mass of the float is much smaller than the added mass of the reaction section, because the circular plate on the reaction section provides a larger added mass effect, as it pushes and pulls a large fluid volume during the heave motion.

The radiation damping of the SRFPA system is shown in Fig. 16b. Clearly, due to far distance from the free surface, the radiation damping for the reaction section almost vanishes across the whole range of wave periods. For the float, nearly the same results as the locked SRFPA (Fig. 10b) are observed. It is apparent, therefore, that the heave motion of float is the dominant source of radiation damping for the SRFPA system. In fact, as mentioned in Ref. [9], the viscous damping induced by the reaction plate, as a result of flow separation and vortex shedding, is the primary damping source for the reaction section.

The BEM derived wave excitation forces for the float and the reaction section are summarized by the wave period dependent amplitude and phase shown in Fig. 17. The excitation force amplitude curves seen in Fig. 17a, as normalized by wave height, show that (i) an increase in wave period increases the excitation force on the float; (ii) it is verified that the excitation force on the float is much larger than on the reaction section, because the motion of fluid particles decreases rapidly with increasing depth below the free surface. In addition, in Fig. 17b, almost zero phase between the excitation force on the float and the incident wave is observed across the whole range of wave periods whereas the phase for the reaction section varies from $-180°$ to $0°$. As the wave period increases, the force phase difference between the float and the reaction section is reduced and it is anticipated that the excitation forces on them will be synchronised with the incident wave when the wave period is sufficiently longer.

4.4 Additional viscous damping

Fluid viscosity has a significant impact on the dynamics of the SRFPA in heave motion, particularly at resonance. To

account for these viscous effects, a drag force is introduced within the present dynamic model. In general, the total drag force includes the form drag as a result of flow separation and vortex shedding, and the friction drag as result of fluid shear stress on body surfaces. As seen in Fig. 15, for the float and the reaction plate, the drag forces should have a much larger proportion of form drag compared to friction drag because of relatively small thickness of hull walls and sharp edges which lead to frequent flow separation. For the central columns, compared to the float and the reaction plate, the drag forces can be negligible due to their streamlined shapes. In this paper, to represent drag forces on the float and the reaction plate, a non-linear drag term is assumed, which is proportional to the square of the velocity and expressed as follows [41,42]

$$F_{\text{drag}} = -\frac{1}{2}\rho A_{\text{s}} C_{\text{d}} \dot{Z} \left|\dot{Z}\right|, \tag{55}$$

where A_{s} is the cross sectional area of the float or the reaction plate perpendicular to the heave direction and C_{d} is the drag coefficient, ρ is the density of water. Note that the absolute value of the velocity term is applied to ensure that the damping force is always in the opposite direction to the velocity. This expression would have been more realistic if the relative velocity between the body and the fluid particles is used instead of the body velocity. However, it is difficult to evaluate the velocity of fluid particles, because the flow around bodies is quite complex in waves.

Generally, the value of drag coefficient depends on the body geometry, the Reynolds number Re (in this problem, $Re \approx 1 \times 10^6 \sim 10 \times 10^6$) and the Keulegan–Carpenter number $KC = 2\pi A/D$, where A is the body motion amplitude and D is the characteristic diameter of body. Similarly, it is more realistic to define Keulegan–Carpenter number if the relative motion amplitude between the body and the fluid particles is used instead of the body motion amplitude. However, as discussed, it is difficult to evaluate the motion of fluid particles around the body. For the present SRFPA system, KC is generally less than 10. Within this range, Graham's study [43] showed that the variation of drag coefficient was primarily induced by the strength of shed vortices. At low Keulegan–Carpenter numbers, he assumed that vortex flow was dominated by the local flow near sharp edges, and the drag coefficient for plates became KC dependent

$$C_{\text{d}} \propto KC^{-1/3}. \tag{56}$$

Based on Graham's assumption [43], we suppose $C_{\text{d},j} = \delta_j KC^{-1/3}$ ($j = 1$ for the float and $j = 2$ for the reaction plate), where the proportional coefficient δ is an empirical coefficient depending on the plate geometry and dimension, and is generally obtained by experimental tests. Because the reaction plate is much thinner than the float, it is clear that vortices are shed more frequently and intensively near edges of the reaction plate. Therefore, the proportional coefficient δ_2 should be larger than δ_1.

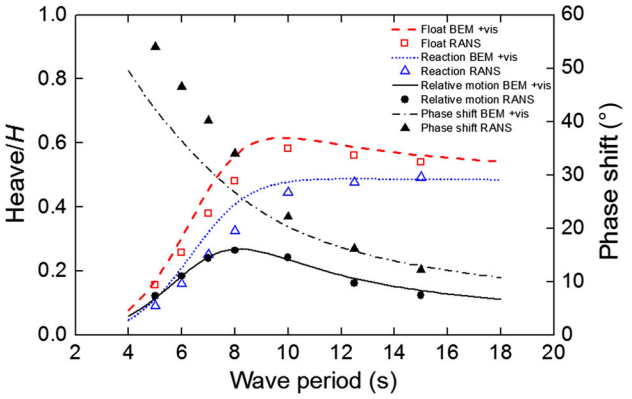

Fig. 18 SRFPA RANS vs. BEM with viscous damping ($\delta_1 = 1.0$, $\delta_2 = 3.5$) derived heave response amplitude (scaled by wave height) and phase ($H = 2.5$ m)

In the frequency domain analysis, the non-linear drag term can be substituted by a linear term using the Lorentz linearization

$$\dot{Z}\left|\dot{Z}\right| \approx \frac{8}{3\pi}\| -\mathrm{i}\omega z\| \,\mathrm{Re}\left(-\mathrm{i}\omega z \mathrm{e}^{-\mathrm{i}\omega t}\right), \tag{57}$$

thus

$$f_{\text{drag},j} = \frac{4\mathrm{i}\omega^2}{3\pi}\rho A_{\text{s},j} C_{\text{d},j} \,\|z_j\| \, z_j. \tag{58}$$

The complex drag force $f_{\text{drag},j}$ ($j = 1$ for the float and $j = 2$ for the reaction plate) is included in the constrained heave Eq. (1). To solve the equation and overcome the nonlinearity, we proceed through an iterative scheme so that a linear problem is solved at each iteration.

4.5 Heave response in waves

Figure 18 shows the RANS and BEM derived heave RAOs of the float and the reaction section, the relative motion and the phase shift between the two bodies in 2.5 m wave height scenarios with a PTO absorption damping of 1200 kN·s/m, where the results are plotted against the wave period. In the present BEM, drag coefficients for the float and the reaction plate are determined by the proportional coefficients $\delta_1 = 1.0$ and $\delta_2 = 3.5$, which is chosen based on the experimental measurements from the wave tank test and the RANS simulation results. Key observations to be made from Fig. 18 are as follows. First, the BEM derived heave RAOs of the float and the reaction section, and the relative motion RAO, agree fairly well with the RANS simulation results. The agreement

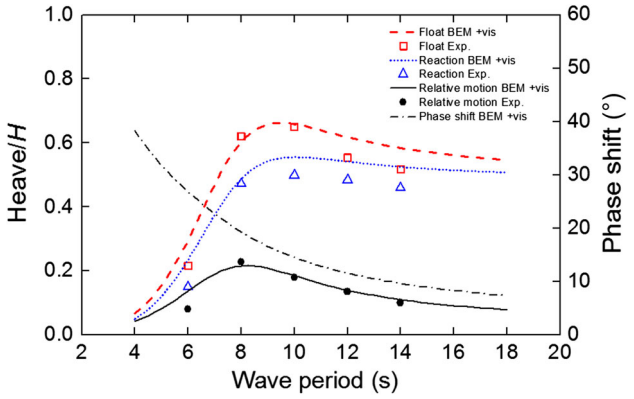

Fig. 19 SRFPA experimental test vs. BEM with viscous damping ($\delta_1 = 1.0, \delta_2 = 3.5$) derived heave response amplitude (scaled by wave height) and phase ($H = 2.5$ m)

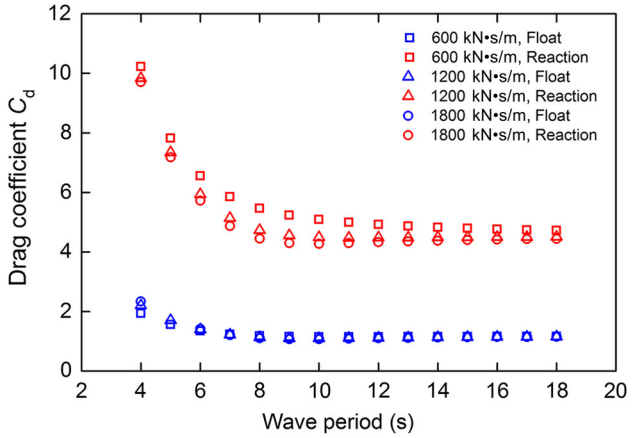

Fig. 20 Drag coefficients for the float and the reaction plate with different PTO damping ($H = 2$ m)

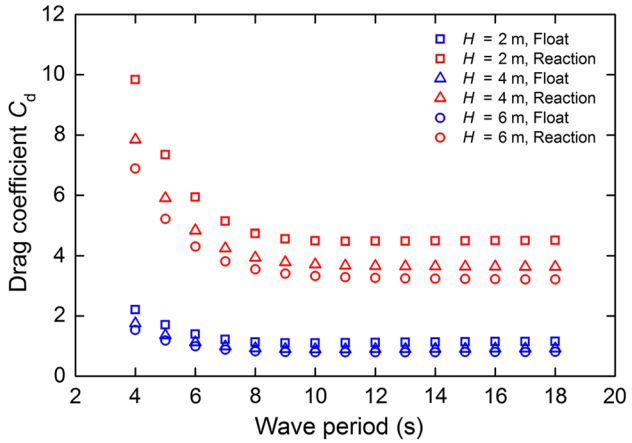

Fig. 21 Drag coefficients for the float and the reaction plate with PTO damping 1200 kNs/m in different wave height scenarios

indicates that the non-linear drag term is capable of representing viscous effects on the SRFPA system. Second, the heave motion of the float section is greater than that of the reaction section, because the wave excitation force on the float is much more larger than on the reaction section, based on the analysis discussed in Sect. 4.3. The heave response of the float has a peak period about $T = 10$ s, whereas the data of the reaction section gradually increase with the incident wave period, and no peak occurs in the heave response, which implies that the reaction section is over-damped. Third, the BEM and RANS results of the phase shift between the float and the reaction section at wave periods less than 8 s, differ by approximately 20%. The difference could be attributed to other non-linear hydrodynamic and damping effects, which are more significant when the wave period is shorter under 2.5 m wave height. The phase shift angle is reduced as the incident wave period increases. It is anticipated that the angle will vanish when the wave period is sufficiently longer while the float and the reaction section will follow the motion of the incident wave. Moreover, the phase shift results in a relative motion peak period about $T = 8$ s, which differs from the peak period of the float.

The experimental and BEM derived heave RAOs of the float and the reaction section, and the relative motion between them in 2.5 m wave height scenarios are shown in Fig. 19. In the wave tank test, the PTO absorption damping was controlled by adjusting the needle valve, and the averaged PTO damping for the results presented in Fig. 19 were about 1800 kN·s/m. Key observations to be made from this figure are as follows. First, the heave RAOs of the float and the reaction section, and the relative motion RAO derived from the present BEM analyses are in general agreement with the experimental results. Second, both heave responses of the float and the reaction section have a peak period $T = 10$ s, and similar trends of responses are observed. Compared to Fig. 18, it is anticipated that the heave motion of the reaction section tends to follow the motion of the float section as the PTO absorption damping increases. Third, the relative motion response between the two bodies is reduced when wave energy is extracted by the PTO mechanism, and it also decreases as the PTO absorption damping increases.

As discussed in Sect. 4.4, the drag coefficients C_d are obtained when the iterative calculation of the motion equation converges. Figures 20 and 21 show the drag coefficients for the float and the reaction plate against the wave period, where the results are plotted across a range of PTO absorption damping (i.e. 600 kN·s/m, 1200 kN·s/m, 1800 kN·s/m) and a range of wave heights (i.e. 2 m, 4 m, 6 m). Key observations to be made from Figs. 20 and 21 are as follows. First, PTO damping and wave height have little effect on C_d for the float whereas, for the reaction plate, it slightly decreases with PTO damping and wave height. Second, at short wave periods, an increase in wave period slightly decreases C_d for the float. A similar trend is evident for the reaction plate: an increase in wave period greatly decreases C_d. In fact, based on Graham's

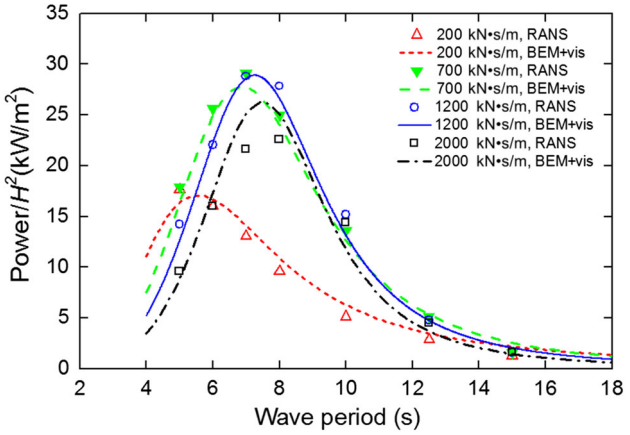

Fig. 22 Power absorption performance (scaled by the square of wave height) of the SRFPA system in 2.5 m wave height scenarios

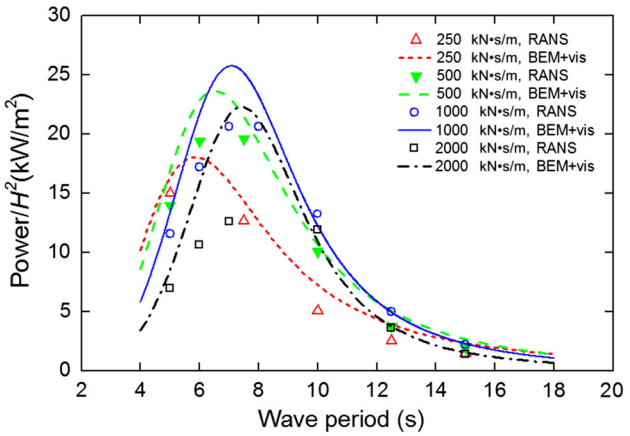

Fig. 23 Power absorption performance (scaled by the square of wave height) of the SRFPA system in 4 m wave height scenarios

assumption [43], C_d increases more rapidly as KC decreases (its variation rate depends on the first-order derivative regarding KC). Clearly, for smaller KC (short wave periods), the variation rate of C_d for the reaction plate is larger than that for the float. These factors above result in the visible trends in Figs. 20 and 21. Third, for the SRFPA system, we can conclude that C_d for the float ranges from about 1 to 1.5 and C_d for the reaction plate ranges from about 3 to 6 in operational wave conditions.

4.6 Wave power absorption

Figures 22 and 23 show the wave power extraction performance of the SRFPA system in 2.5 m and 4 m wave height scenarios against wave period across a range of PTO absorption damping between 200 kN·s/m and 2000 kN·s/m, where the present BEM prediction is compared to the RANS simulation data. Key observations to be made from Figs. 22 and 23 are as follows. First, after we introduce the viscous damping, the BEM results agree well with the RANS calculated values in 2.5 m wave height scenarios whereas, in 4 m wave height scenarios, the BEM derived power is greater than the RANS results near resonance. The difference can be attributed to other non-linear hydrodynamic effects, wave overtopping and re-entering impact of out-of-water for the float. In the RANS simulations, particularly near resonance, wave overtopping and re-entering impact of out-of-water for the float we observed in 4 m wave height scenarios occurred much more frequently than that in 2.5 m wave height scenarios, which generally result in additional damping forces that restrain the SRFPA motion and reduce wave power output. This reveals that, in large wave height scenarios, wave overtopping and re-entering impact of out-of-water phenomena, as complex interaction effects between waves and the SRFPA system, are the more significant damping source, but our dynamic model does not account for these effects. Second, short peak period is observed for small values of PTO absorption damping. It is anticipated that the peak period of wave power output decreases as PTO absorption damping decreases. Third, the SRFPA system have an optimal power extraction performance when the PTO damping is in the range between 700 kN·s/m and 1200 kN·s/m. In Fig. 23, the maximum time-averaged power 330 kW in 4 m wave height scenarios is generated by the SRFPA system when the PTO damping is equal to 1000 kN·s/m.

5 Discussion

In this section, the power absorption efficiency of the SRFPA system will be discussed. Based on the optimum radiation pattern for heaving single-body point absorbers in ideal potential flow, a well known upper bound on the power capture was derived by Evans [44]. Here J denotes the wave energy flux per unit length of wave crest (W/m), λ and T are the incident wave length and period, respectively.

$$P \leqslant P_{\max} = \frac{J}{k_0} = \frac{J\lambda}{2\pi}, \tag{59}$$

$$J = \frac{\rho g^2 T H^2 \tanh(k_0 h)}{32\pi}\left[1 + \frac{2k_0 h}{\sinh(2k_0 h)}\right]. \tag{60}$$

For a given FPA geometry, it is clear that the maximum wave power absorption $P_{\max}$ and a capture width $\lambda/2\pi$ can be reached when the system is at resonance. Falnes' study [29] showed that, for a two-body axisymmetric system, it is possible to extract same amount of wave energy as a single-body system. If we assume that the spring stiffness of the PTO is equal to zero, as seen in the motion equation (2), the optimum PTO damping for different incident wave frequencies is determined by

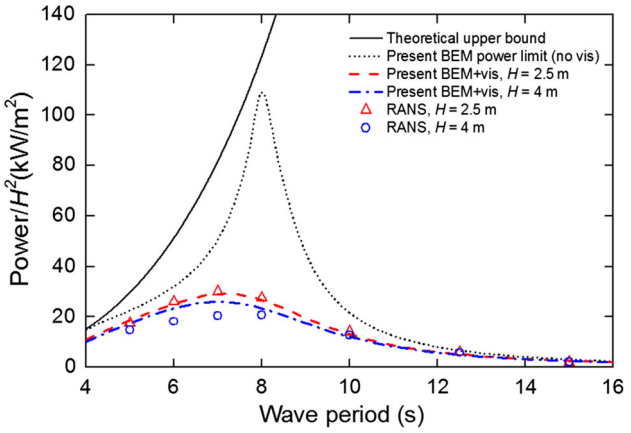

Fig. 24 Maximum power absorption of the SRFPA system for different incident wave periods

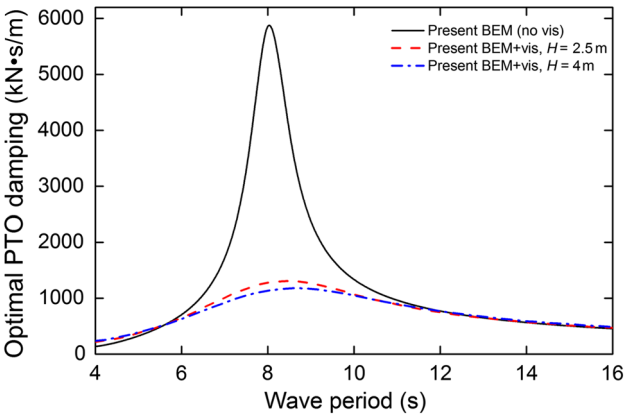

Fig. 25 Optimal absorption damping of the PTO calculated by the present BEM

$$c_{\mathrm{pto}}^{\mathrm{opt}} = \frac{1}{\omega}\left\| \frac{K_1 K_2}{K_1 + K_2} \right\|. \tag{61}$$

We can obtain the potential flow power extraction limit for the SRFPA system from Eq. (61) by using the present inviscid BEM solver. Moreover, the optimal absorbed wave power predicted from the present BEM with additional viscous drag and from the RANS simulations [28] are also presented, where the optimal solutions are determined by selecting the PTO damping to provide the maximum power extraction performance for each wave period. A comparison is shown in Fig. 24 to illustrate the difference between these solutions. When viscosity is neglected, a maximum wave power extraction of the SRFPA system across the whole range of wave periods is obtained at the resonant period of 8 s, which is close to the power upper bound. Meanwhile, at wave periods except resonant period, it is apparently impossible for the SRFPA system to approach to the power upper bound even if the optimal PTO absorption damping is selected. However, in the presence of viscous drag, other non-linear wave and wave-body interaction-induced damping forces, the power extraction efficiency from waves is in reality much lower than the results from the inviscid BEM analysis, particularly near resonance. In addition, as shown in Fig. 24, both results from the BEM analysis with additional viscous drag and the RANS simulations exhibit lower power extraction efficiency in 4 m waves than that in 2.5 m waves, which reveals that viscous drag and these non-linear interaction effects between waves and the SRFPA system result in more wave energy dissipated in larger wave height scenarios, where wave overtopping and the re-entering impact of out-of-water for the SRFPA system are frequently observed and actually become the dominant damping sources. In general, the viscous drag induced by flow separation and vortex shedding, the wave overtopping and the re-entering impact of out-of-water induced by wave-body interactions, both highly depend on specific wave scenarios and FPA designs. Therefore, it is difficult to quantity these effects on power output using the present BEM.

Figure 25 shows the optimal PTO absorption damping for the SRFPA system at each wave period using the present BEM. Near resonance, across a range of wave periods 7–10 s, the inviscid BEM analysis derived optimal PTO damping is much larger than that derived from the BEM with viscous drag. This could be attributed to the drag force induced by flow separation and vortex shedding, which dissipates a large proportion of wave energy. Then only much lower PTO damping is needed to convert the remaining proportion of wave energy into useful power. This reveals that viscous drag has a significant effect on the selection of PTO absorption damping, which should be carefully considered in FPA designs.

6 Conclusions

We develop a frequency domain boundary element method for the inviscid hydrodynamic analyses of wave-body interactions. The method is based on the free-surface Green's function and the constant panel method. The key numerical issues in the evaluation of the Green's function and the influence coefficient matrices are also discussed. The inviscid hydrodynamic results for a floating hemisphere in heave derived from the present BEM solver is validated by the theoretical and numerical solutions [38,39]. Two-body SRFPA wave energy conversion systems are analysed using a linear, heave constrained dynamic model with a simplified PTO mechanism, where the validated BEM solver is used to obtain the inviscid hydrodynamic results. Experimental wave tank tests and RANS simulations of locked and unlocked SRFPA system models in regular waves were performed [28]. The viscous damping induced by flow separation and vortex shedding from sharp edges of the SRFPA system is treated as a quadratic drag term, where we assume that the drag coefficient is determined by the Keulegan–Carpenter number. The

heave response and the power absorption performance of the SRFPA system model under various wave conditions predicted by the present BEM with viscous drag are validated with the experimental data and RANS simulation results.

In our algorithms for the free-surface Green's function, 30 Gauss–Laguerre sampling points are used in the integral method to keep balance between the numerical accuracy and the computational efficiency. The series method converges faster in far field and has a singularity problem in near field, the computational efficiency of which primarily depends on the ratio R/h. The CPU time shows a critical value 0.1 of R/h: the integral method consumes much less computational time below 0.1, and so does the series method above 0.1. Based on this discovery, a time-saving strategy is adopted in the present BEM solver.

Comparative results show that the inviscid hydrodynamic analyses of the SRFPA model using the present BEM lead to notable over-prediction of heave response amplitudes and wave power output near resonance, where viscous damping and non-linear hydrodynamic loads could have significant influence on the SRFPA system. After the viscous drag term is included, our hydrodynamic model with the BEM derived predicted results of heave responses and power extraction performance of the SRFPA agree well with the experimental measurements and the RANS simulation results in smaller wave height scenarios, where the viscous drag force induced by flow separation and vortex shedding is the dominant damping source. When the wave height is larger, our predicted results compare well with the RANS simulation results over a broad range of incident wave periods, but exhibit larger values near resonance. In reality, the wave overtopping and the re-entering impact of out-of-water for the SRFPA occur frequently and become more significant in larger wave height scenarios, but it is difficult to account for these complex nonlinear effects in our hydrodynamic model.

Acknowledgements We would like to acknowledge the National Natural Science Foundation of China (Grants 51479114, 51761135012) for supporting this work.

Appendix

In the present BEM, all body surface boundaries are subdivided into a number of curved surfaces, which are approximated by spatial quadrilateral panels or triangular panels. As seen in Fig. 4, the centroid $P_c(x_c, y_c, z_c)$ of each panel element is represented as

$$x_c = \frac{\sum_{k=1}^{n} x_k}{n}, \quad y_c = \frac{\sum_{k=1}^{n} y_k}{n}, \quad z_c = \frac{\sum_{k=1}^{n} z_k}{n}, \tag{A1}$$

where $A_k(x_k, y_k, z_k)$ represents the k-th node of the panel element, especially $n = 3$ for triangular panels, $n = 4$ for quadrilateral panels.

Without losing generality, assuming the unit normal vector $\boldsymbol{n}$ of the panel element directed from the fluid into bodies, for triangular panels, it can be evaluated by

$$\boldsymbol{n} = \frac{\boldsymbol{A}_1\boldsymbol{A}_2 \times \boldsymbol{A}_2\boldsymbol{A}_3}{|\boldsymbol{A}_1\boldsymbol{A}_2 \times \boldsymbol{A}_2\boldsymbol{A}_3|}, \tag{A2}$$

for quadrilateral panels,

$$\boldsymbol{n} = \frac{\boldsymbol{A}_1\boldsymbol{A}_3 \times \boldsymbol{A}_2\boldsymbol{A}_4}{|\boldsymbol{A}_1\boldsymbol{A}_3 \times \boldsymbol{A}_2\boldsymbol{A}_4|}. \tag{A3}$$

In general, the four nodes of a spatial quadrilateral panel are probably not located on the same plane, which makes it useless in the present BEM. One treatment is applied here: the whole panel element $A_1A_2A_3A_4$ is projected to a plane (perpendicular to the normal vector $\boldsymbol{n}$ and contains the centroid P_c), then it is approximately replaced by the projective element $A_1'A_2'A_3'A_4'$.

For convenience, the local coordinate system $P_c - \alpha\beta\gamma$ on each panel element is established to evaluate the influence coefficient matrices. On an arbitrary panel element $\triangle S_j$, the centroid $P_c(x_c, y_c, z_c)$ is specified as the origin and let $\boldsymbol{\tau}_\alpha$, $\boldsymbol{\tau}_\beta, \boldsymbol{\tau}_\gamma$ signify the basis vectors of $P_c - \alpha\beta\gamma$. We can choose an arbitrary node $A_k(x_k, y_k, z_k)$ of the element to determine the basis vector $\boldsymbol{\tau}_\alpha$

$$\boldsymbol{\tau}_\alpha = \frac{\boldsymbol{P}_c\boldsymbol{A}_k}{|\boldsymbol{P}_c\boldsymbol{A}_k|}, \tag{A4}$$

and

$$\boldsymbol{\tau}_\gamma = \boldsymbol{n}, \quad \boldsymbol{\tau}_\beta = \boldsymbol{\tau}_\gamma \times \boldsymbol{\tau}_\alpha. \tag{A5}$$

Let $\boldsymbol{\tau}_\alpha$, $\boldsymbol{\tau}_\beta$, $\boldsymbol{\tau}_\gamma$ be column vectors, thus an orthogonal coordinate-transformation matrix can be obtained

$$\boldsymbol{C}_t = (\boldsymbol{\tau}_\alpha, \boldsymbol{\tau}_\beta, \boldsymbol{\tau}_\gamma)^{\mathrm{T}}, \tag{A6}$$

then the transformation relation between the coordinates (x, y, z) in $O - xyz$ and (α, β, γ) in $P_c - \alpha\beta\gamma$ is represented as

$$\begin{pmatrix}\alpha\\ \beta\\ \gamma\end{pmatrix} = \boldsymbol{C}_t \begin{pmatrix}x - x_c\\ y - y_c\\ z - z_c\end{pmatrix}, \qquad \begin{pmatrix}x\\ y\\ z\end{pmatrix} = \boldsymbol{C}_t^{\mathrm{T}} \begin{pmatrix}\alpha\\ \beta\\ \gamma\end{pmatrix} + \begin{pmatrix}x_c\\ y_c\\ z_c\end{pmatrix}, \tag{A7}$$

On the element $\triangle S_j$, a bilinear transformation between the coordinates (α, β) in the local system $P_c - \alpha\beta\gamma$ and (u, v) on the standard square E_j^s is used here

$$\alpha(u,v) = \bar{\alpha} + a_\alpha u + b_\alpha v + c_\alpha uv, \tag{A8}$$

$$\beta(u,v) = \bar{\beta} + a_\beta u + b_\beta v + c_\beta uv, \tag{A9}$$

where

$$\bar{\alpha} = \frac{1}{4}\sum_{k=1}^{4}\alpha_k, \quad a_\alpha = \bar{\alpha} - \frac{1}{2}(\alpha_2+\alpha_3), \tag{A10}$$
$$b_\alpha = \bar{\alpha} - \frac{1}{2}(\alpha_3+\alpha_4), \quad c_\alpha = \bar{\alpha} - \frac{1}{2}(\alpha_2+\alpha_4),$$

$$\bar{\beta} = \frac{1}{4}\sum_{k=1}^{4}\beta_k, \quad a_\beta = \bar{\beta} - \frac{1}{2}(\beta_2+\beta_3), \tag{A11}$$
$$b_\beta = \bar{\beta} - \frac{1}{2}(\beta_3+\beta_4), \quad c_\beta = \bar{\beta} - \frac{1}{2}(\beta_2+\beta_4),$$

where (α_k, β_k) represents the local coordinates of the k-th node on the element $\triangle S_j$. The Jacobian determinant associated with the transformation of the element $\triangle S_j$ to its image E_j^s is evaluated by

$$J(u,v) = \left|\frac{D(\alpha,\beta)}{D(u,v)}\right| = a_\alpha b_\beta - b_\alpha a_\beta + (a_\alpha c_\beta - c_\alpha a_\beta)u + (c_\alpha b_\beta - b_\alpha c_\beta)v, \tag{A12}$$

For triangular panel elements, the transformation Eqs. (A8) and (A9) are no longer applicable. Without losing generality, assuming the nodes A_3 and A_4 of the element coinciding, we apply a linear transformation

$$\alpha(u,v) = \bar{\alpha} + a_\alpha u + b_\alpha v, \tag{A13}$$

$$\beta(u,v) = \bar{\beta} + a_\beta u + b_\beta v, \tag{A14}$$

where

$$\bar{\alpha} = \frac{1}{2}(\alpha_1+\alpha_3), \quad a_\alpha = \frac{1}{2}(\alpha_1-\alpha_2), \quad b_\alpha = \frac{1}{2}(\alpha_2-\alpha_3), \tag{A15}$$

$$\bar{\beta} = \frac{1}{2}(\beta_1+\beta_3), \quad a_\beta = \frac{1}{2}(\beta_1-\beta_2), \quad b_\beta = \frac{1}{2}(\beta_2-\beta_3), \tag{A16}$$

and the Jacobian determinant becomes

$$J(u,v) = \left|\frac{D(\alpha,\beta)}{D(u,v)}\right| = a_\alpha b_\beta - b_\alpha a_\beta. \tag{A17}$$

References

1. Salter, S.H.: Wave power. Nature **249**, 720–724 (1974)
2. Ocean Power Technologies (2011) May [Online]. http://www.oceanpowertechnologies.com
3. Weber, J., Mouwen, F., Parish, A., et al.: Wavebob-research & development network and tools in the context of systems engineering. In: Proceedings of the Eighth European Wave and Tidal Energy Conference (2009)
4. Salter, S.H., Lin, C.P.: The sloped IPS wave energy converter. In: Proceedings of the 2nd European Wave Energy Conference, pp. 337–344 (1995)
5. Payne, G.S., Taylor, J.R.M., Bruce, T., et al.: Assessment of boundary-element method for modelling a free floating sloped wave energy device. Part 1. Numerical modelling. Ocean Eng. **35**, 333–341 (2008)
6. Payne, G.S., Taylor, J.R.M., Bruce, T., et al.: Assessment of boundary-element method for modelling a free-floating sloped wave energy device. Part 2. Experimental validation. Ocean Eng. **35**, 342–357 (2008)
7. Xu, Y., Dong, W.C.: Numerical study on wave loads and motions of two ships advancing in waves by using 3D translating–pulsating source. Acta. Mech. Sin. **29**, 494–502 (2013)
8. Zhou, B.Z., Ning, D.Z., Teng, B., et al.: Fully nonlinear modeling of radiated waves generated by floating flared structures. Acta. Mech. Sin. **30**, 667–680 (2014)
9. Beatty, S.J., Hall, M., Buckham, B.J., et al.: Experimental and numerical comparisons of self-reacting point absorber wave energy converters in regular waves. Ocean Eng. **104**, 370–386 (2015)
10. Rahmati, M.T., Aggidis, G.A.: Numerical and experimental analysis of the power output of a point absorber wave energy converter in irregular waves. Ocean Eng. **111**, 483–492 (2016)
11. Sergiienko, N.Y., Cazzolato, B.S., Ding, B., et al.: Performance comparison of the floating and fully submerged quasi-point absorber wave energy converters. Renew. Energy **108**, 425–437 (2017)
12. Kurniawan, A., Chaplin, J.R., Greaves, D.M., et al.: Wave energy absorption by a floating air bag. J. Fluid Mech. **812**, 294–320 (2016)
13. Li, Y., Yu, Y.H.: A synthesis of numerical methods for modeling wave energy converter-point absorbers. Renew. Sustain. Energy Rev. **16**, 4352–4364 (2012)
14. Bjarte-Larsson, T., Falnes, J.: Laboratory experiment on heaving body with hydraulic power take-off and latching control. Ocean Eng. **33**, 847–877 (2006)
15. Piscopo, V., Benassai, G., Cozzolino, L., et al.: A new optimization procedure of heaving point absorber hydrodynamic performances. Ocean Eng. **116**, 242–259 (2016)
16. Ding, B., Cazzolato, B.S., Arjomandi, M., et al.: Sea-state based maximum power point tracking damping control of a fully submerged oscillating buoy. Ocean Eng. **126**, 299–312 (2016)
17. Ding, B., Sergiienko, N., Bleckly, B., et al.: Power-take-off control in a scaled experiment of a point absorber wave energy converter. In: Proceeding of the European Wave and Tidal Energy Conference (2017)
18. Sergiienko, N., Cazzolato, B., Hardy, P., et al.: Internal-model-based velocity tracking control of a submerged three-tether wave energy converter. In: Proceeding of the European Wave and Tidal Energy Conference (2017)
19. Beatty, S., Ferri, F., Bocking, B., et al.: Power take-off simulation for scale model testing of wave energy converters. Energies **10**, 973 (2017)
20. Sinha, A., Karmakar, D., Soares, C.G., et al.: Performance of optimally tuned arrays of heaving point absorbers. Renew. Energy **92**, 517–531 (2016)
21. WAMIT Inc.: Version7.0 (2012). http://www.wamit.com

22. Hulme, A.: The heave added-mass and damping coefficients of a submerged torus. J. Fluid Mech. **155**, 511–530 (1985)
23. Newman, J.N.: Double-precision evaluation of the oscillatory source potential. J. Ship Res. **28**, 151–154 (1984)
24. Newman, J.N.: Algorithms for the free-surface Green function. J. Eng. Math. **19**, 57–67 (1985)
25. Newman, J.N.: The approximation of free-surface green functions. In: Retirement Meeting for Professor F.J. Ursell, Manchester, UK, 29–30 (1990)
26. Yao, X.L., Sun, S.L., Wang, S.P., et al.: The research on the highly efficient calculation method of 3-D frequency-domain Green function. J. Mar. Sci. Appl. **8**, 196–203 (2009)
27. Chen, X.B.: Hydrodynamics in offshore and naval applications part 1. In: Proceedings of the 6th International Conference on Hydrodynamics (2004)
28. Yu, Y.H., Li, Y.: Reynold-Averaged Navier–Stokes simulation of the heave performance of a two-body floating-point absorber wave energy system. Comput. Fluids **73**, 104–114 (2013)
29. Falnes, J.: Wave-energy conversion through relative motion between two single-mode oscillating bodies. J. Offshore Mech. Arct. Eng. **121**, 32–38 (1999)
30. Wehausen, J.V., Laitone, E.V.: Surface Waves. Springer, Berlin (1960)
31. Endo, H.: Numerical evaluation of principal value integral by Gauss–Laguerre quadrature. AIAA J. **21**, 149–151 (1983)
32. Li, L.: Numerical seakeeping predictions of shallow water effect on two ship interactions in waves. [Ph.D. Thesis], Dalhousie University, Canada (2001)
33. Abramowitz, M., Stegun, I.A.: Handbook of Mathematical Functions with Formulas, Graphs, and Mathematical Tables. Dover Publications, New York (1972)
34. Liu, R.M., Ren, H.L., Li, H.: An improved Gauss–Laguerre method for finite water depth green function and its derivatives. J. Ship Mech. **12**, 188–196 (2008) (in Chinese)
35. John, F.: On the motion of floating bodies II. Commun. Pure Appl. Math. **3**, 45–101 (1950)
36. Havelock, T.: Waves due to a floating sphere making periodic heaving oscillations. Proc. R. Soc. A Math. Phys. Eng. Sci. **231**, 1–7 (1955)
37. Dai, Y.S., Duan, W.Y.: Potential Flow Theory of Ship Motions in Waves. National Defence and Industry Publishing House, Beijing (2008) (in Chinese)
38. Hulme, A.: The wave forces acting on a floating hemisphere undergoing forced periodic oscillations. J. Fluid Mech. **121**, 443–463 (1982)
39. Chen, X.B., Diebold, L., Doutreleau, Y.: New Green-function method to predict wave-induced ship motions and loads. In: Proceedings of the Twenty-Third Symposium on Naval Hydrodynamics (2000)
40. Li, Y., Yu, Y.H., Epler, J., et al.: Experimental investigation of the power generation performance of floating-point absorber wave energy systems. In: 27th International Workshop on Water Waves and Floating Bodies, Copenhagen, Denmark (2012)
41. Eidsmoen, H.: Simulation of a slack-moored heaving-buoy wave-energy converter with phase control. Norwegian University of Science and Technology, Trondheim, Norway, Technical Report (1996)
42. Tao, L., Cai, S.: Heave motion suppression of a Spar with a heave plate. Ocean Eng. **31**, 669–692 (2004)
43. Graham, J.M.R.: The forces on sharp-edged cylinder in an oscillatory flow at low Keulegan–Carpenter numbers. J. Fluid Mech. **97**, 331–346 (1980)
44. Evans, D.: A theory for wave-power absorption by oscillating bodies. J. Fluid Mech. **77**, 1–25 (1976)